Stähler, S. C., Khan, A., Banerdt, W. B., Lognonné, P., Giardini, D., Ceylan, S., Drilleau, M., Garcia, R. F., Duran, A. C., Huang, Q., Kim, D., Lekić, V., Samuel, H., Schimmel, M., Schmerr, N., Sollberger, D., Stutzmann, É., Xu, Z., Charalambous, C., ... Smrekar, S. (2021). Seismic detection of the martian core. *Science*, *373*(6553), 443-448. https://doi.org/10.1126/science.abi7730

# Title: Seismic detection of the Martian core

**Authors:** Simon C. Stähler*[1], Amir Khan[1,2], W. Bruce Banerdt[3], Philippe Lognonné[4], Domenico Giardini[1], Savas Ceylan[1], Mélanie Drilleau[5], A. Cecilia Duran[1], Raphaël F. Garcia[5], Quancheng Huang[6], Doyeon Kim[6], Vedran Lekic[6], Henri Samuel[4], Martin Schimmel[7], Nicholas Schmerr[6], David Sollberger[1], Éléonore Stutzmann[4], Zongbo Xu[4], Daniele Antonangeli[8], Constantinos Charalambous[9], Paul Davis[10], Jessica C.E. Irving[11], Taichi Kawamura[4], Martin Knapmeyer[12], Ross Maguire[6], Angela G. Marusiak[3], Mark P. Panning[3], Clément Perrin[13], Ana-Catalina Plesa[12], Attilio Rivoldini[14], Cédric Schmelzbach[1], Géraldine Zenhäusern[1], Éric Beucler[13], John Clinton[15], Nikolaj Dahmen[1], Martin van Driel[1], Tamara Gudkova[16], Anna Horleston[11], W. Thomas Pike[9], Matthieu Plasman[4], Suzanne E. Smrekar[3]

**Affiliations:**

[1]Institute of Geophysics, ETH Zürich; Zürich, Switzerland

[2]Physik-Institut, University of Zürich; Zürich, Switzerland

[3]Jet Propulsion Laboratory, California Institute of Technology; Pasadena CA, USA

[4]Université de Paris, Institut de physique du globe de Paris, CNRS, 75005 Paris

[5]Institut Supérieur de l'Aéronautique et de l'Espace SUPAERO; Toulouse, France

[6]Department of Geology, University of Maryland; College Park, MD 20742 USA

[7]Geosciences Barcelona – CSIC; Barcelona, Spain

[8]Sorbonne Université, Muséum National d'Histoire Naturelle, UMR CNRS 7590, Institut de Minéralogie, de Physique des Matériaux et de Cosmochimie, IMPMC; Paris, France

[9]Department of Electrical and Electronic Engineering, Imperial College; London, United Kingdom

[10]Department of Earth, Planetary, and Space Sciences, University of California Los Angeles; Los Angeles, USA

[11]School of Earth Sciences, University of Bristol; Bristol, United Kingdom

[12]DLR Institute of Planetary Research; Berlin, Germany

[13]Laboratoire de Planétologie et Géodynamique, Univ. Nantes; Nantes, France

[14]Royal Observatory of Belgium; Brussels, Belgium

[15]Swiss Seismological Service (SED), ETH Zürich; Zürich, Switzerland

[16]Schmidt Institute of Physics of the Earth RAS; Moscow, Russia

*Corresponding author. Email: simon.staehler@erdw.ethz.ch

**Abstract:** Clues to a planet's geologic history are contained in its interior structure, particularly its core. We detected reflections of seismic waves from the core-mantle boundary of Mars using InSight seismic data and invert these together with geodetic data to constrain the radius of the liquid metal core to 1830±40 km. The large core implies a Martian mantle mineralogically

similar to the terrestrial upper mantle and transition zone, but differs from the Earth by not having a bridgmanite-dominated lower mantle. We inferred a mean core density of 5.7 g/cm$^3$ to 6.3 g/cm$^3$, requiring a substantial complement of light elements dissolved in the iron-nickel core. The seismic core shadow covers half the surface of Mars, including the majority of potentially active regions, e.g., Tharsis, possibly limiting the number of detectable marsquakes.

**One-Sentence Summary:** Marsquake observations confirm a large, liquid, and light Martian metal core.

**Main Text:**

The core of a planet plays a prominent role because it governs many of the fundamental processes from dynamo action and magnetic field generation to mantle convection that impact the surface through volcanic and tectonic activity, and may influence the early climate through magnetic shielding of the atmosphere. The size of the Martian core is of particular interest because of its dramatic impact on the planet's evolution, which differs from the Earth's primarily as a result of Mars' smaller size, and therefore, accelerated differentiation and core formation and cooling-off that resulted a rigid-shell one-plate planet (*1*, *2*). A small core with a radius between 1300-1600 km would be deficient in light elements and accommodate a Martian lower mantle similar to the Earth's, dominated by bridgmanite-structure silicates (*3*); a large core with a radius range between 1800-1900 km would instead be enriched in light elements, exclude the presence of lower mantle layer (*4*), and thereby exert a markedly different dynamic control over the Martian mantle (*5–8*) with implications for an early Martian dynamo (*1*) that could explain the observed highly magnetized crust in the southern highlands (*9*). Direct constraints on the core and deep interior of Mars, however, are scarce and limited to global geophysical measurements, including mass, moment of inertia, and tidal response (*10*, *11*), in addition to geochemical data based on achondritic basaltic meteorites that originated from the surface of Mars (*12–14*). Collectively, these observations suggest a liquid core with a radius in the range ~1700-1900 km (*4*, *8*, *11*, *15*, *16*). However, without additional observations the range of potential Martian core sizes encompasses a large enough range to allow for either the presence or the absence of a phase transition equivalent of the "660-km" discontinuity that marks the onset of the Earth's lower mantle.

The estimate of core size can be improved with the direct detection of core-interacting seismic phases, which constrain the core size of the Earth and Moon. The Earth's core had been predicted in the late 18th century, based on the recognition that the density of near-surface rocks is substantially lower than the average density of the Earth (*17*), but was not confirmed until global observations of earthquakes became possible (*18*). Subsequent seismic measurements led to the unexpected discoveries in Earth's deep interior, such as the inner core (*19*) and deep mantle layering (*20*, *21*). Similarly, the Apollo lunar seismic data (*22*) were used to establish the existence of a lunar core, including an inner core (*23*, *24*). The detection of seismic waves reflected from the core therefore not only stands to refine the insights gained from studying the chemistry of the Martian rocks, whose siderophile element depletion and isotopic signature point to a core-forming event early in Mars' history (*25*, *26*), but to considerably improve our understanding of the deep interior of Mars.

After a full Martian year, the Interior Exploration using Seismic Investigations, Geodesy and Heat Transport (InSight) mission (*27*) and its seismometer SEIS (*28*) has recorded a multitude of seismic events, which have been located and classified by the Marsquake Service (*29–31*). Of these, the low-frequency events with main energy below 1 Hz and waves travelling through the mantle, can be used to characterize the crustal and mantle structure of Mars (*32*, *33*).
To investigate the core of Mars, we analyzed seismic data from 11 low-frequency marsquakes. Six of them were found in a suitable distance range (27°-38.5° (*30*)), with high enough signal-to-noise ratio (SNR) to identify potential core-reflected S-waves (ScS, see Table 1). Because S-waves cannot propagate in a fluid medium, the core-mantle-boundary (CMB) acts as a polarization filter, reflecting horizontally polarized S-waves (SH waves) back into the mantle, while vertically polarized S-waves (SV) lose some energy due to S-to-P conversion. S-waves

reflected from the CMB are therefore expected to be predominantly horizontally polarized at the receiver, with an azimuth orthogonal to the source direction. The events for which the direction could be determined from P- and S-wave polarization (S0173a and S0235b) appear to originate in the Cerberus Fossae graben system (*29*, *34*), with backazimuths of 70°-90°. The focal mechanisms inferred for these events confirmed normal faulting (*35*), resulting in relatively strong radiation of SH waves towards the core.

All marsquakes show an S-wave coda dominated by receiver-side scattering (Fig. 1A) (*31*). Within this coda, the marsquake with the highest SNR observed so far (S0173a) shows a peak around 510 s and 350 s after the main P- and S-wave arrivals, respectively. We used polarization filtering (*36*) to enhance signals that are linearly and horizontally polarized, as expected for ScS waves (Fig. 1A). After filtering, we observed matching signals for five other events (S0235b, S0407a, S0409d, S0484a, and S0325a) at a similar distance (Fig. 1B). To identify energy pulses that are consistent with ScS, we performed a slant stack (*37*) for the events, using predicted travel times in 5000 mantle models compatible with surface reflected seismic body waves (*32*). The stack of energy in a 10 s time window (filtered between 0.3-0.8 Hz) around the predicted ScS arrival time shows the presence of a signal (Fig. 1C), where a reflection from a ~1600-km depth interface is expected. This result is confirmed by a model-agnostic vespagram-stack showing a low-slowness, steep incidence-angle arrival compatible with a deep reflector (*38*). To refine the arrival time estimate, the time window identified in the stacking was further examined using two independent methods: (i) Manual picking in polarization-filtered filter banks to recognize potential artefacts from instrument or wind and (ii) Coda correlation, using the S-waveform as matching filter, assuming that the S-wave train has high similarity to ScS (*38*). This resulted in a set of picks for each event (Fig 1D). The results from the two methods were compared to the event slant-stacks to remove misidentified signals and consolidated into a single set of picks (Table 1).

While the SNR of the ScS phases is around 2 or less, the signal is significant compared to the energy of the S-wave coda, wind noise, and known instrument artefacts (*38*, *39*). From travel time tables computed in seismic velocity models compatible with observations so far (*8*, *32*, *40*), no other seismic phase is predicted to arrive this late in the seismogram with similar move-out and polarization. Love waves travelling along the surface would have similar polarization, but arrive much earlier and show a large move-out and dispersion. Multiply-reflected body waves should also arrive earlier. We therefore interpreted this signal as an S-wave reflection from the core-mantle-boundary (CMB) that, when using seismic velocity models from (*32*), corresponds to a core with a radius in the range 1770 to 1890 km. We also searched for other phases such as core-reflected P-waves (PcP), but were unable to find consistent arrivals. This was not unexpected due to the lower P-wave reflection coefficient at the CMB. A shear wave that is converted into a P-wave at the CMB (ScP) is predicted to arrive 290 seconds after P for S0325a and we observed a weak phase by correlation analysis. This arrival is only 2 seconds after the identified SSS arrival reported in (*32*), so the peak, while consistent, is not used for inversion here. For four of the six events we investigated, (*32*) reports a second arrival within 20 seconds after the main S-wave. We considered these secondary arrivals to be the depth phase (sS), resulting in marsquakes that occur in the depth range 20-35 km.

The spectral character and the travel time of the direct S-wave for the most distant event (S0167b) located to date (*30*, *32*) was consistent with and comparable to that of the ScS phase (Fig. S6-1) (*38*). This supports the identification of the latter as a core-reflection that has traversed the entire attenuating mantle. The attenuation-corrected power of the ScS phases is below that of the corresponding S-wave arrivals by 10-20 dB. This value is slightly below the ray-theoretical prediction from geometrical spreading (Fig. S6-2) (*38*), assuming full reflection of SH waves at the CMB, possibly due to scattering at other interfaces and three-dimensional structure.

With the identification of the ScS phase, we picked arrival times of the peak energy for each event (Table 1) and inverted those together with the arrival times of P, S, PP, SS, PPP, SSS from (*32*) for mantle P- and S-wave velocity and density, epicentral distance for all considered events, and radius and mean density of the core. We conducted three separate inversions that relied on a pure seismic parameterization, and two mineralogically constrained inversions: a *geodynamic* (*41*, *42*) and a *geophysical* parameterization (*4*). The seismic parameterization considers a layered model of Mars described by P- and S-wave velocity gradients, respectively. The *geodynamic* parameterization depends on quantities that influence the thermo-chemical evolution of the planet and accounts for 4.5 Gyr of planetary evolution. The *geophysical* parameterization relies on a unified description of phase equilibria, seismic properties, and thermo-chemical parameters. The parameterizations (*38*) reflect, in going from seismic over geodynamic to geophysical parameterization, a decrease in the number of degrees of freedom, as the two latter parameterizations depend increasingly on mineral physics information, and therefore better resolved parameters. In the geophysical and geodynamic inversions, we included geodetic data in the form of the degree-2 Love number (*11*), mean density (*16*), and mean moment of inertia (*11*). Because the mean density of the core depends on that of the mantle and therefore on the bulk mantle composition, we considered six different model Martian compositions (*12*, *14*, *43–47*) as part of the geophysical inversion. To solve the inverse problem, we employed a stochastic algorithm (*48*) that samples models fitting the differential body wave travel times within uncertainties and are consistent with prior information (*38*).

We plotted the results from the joint inversion of the differential body wave travel times and the geophysical data (Fig. 2). The S-wave velocity profiles (Fig. 2A) we obtained from the three parameterizations were found to be in good agreement. More scatter exists in the P-wave velocity profiles, which reflects fewer P-wave observations, and structure is only constrained to 800 km depth (Fig. 2A). All parameterizations provide a good fit to the ScS-P travel time observations (Fig. 2B). Above 800 km depth, the velocity profiles are similar to those obtained by the upper mantle inversion (*32*) and below, the S-wave velocity profiles show a distinct increase around 1050 km depth, equivalent of the “410-km” seismic discontinuity in Earth’s mantle that marks the onset of the mantle transition zone, where the dominant upper mantle mineral olivine transforms to wadsleyite. The core-mantle-boundary occurs between 1520-1600 km depth, corresponding to core-mantle-boundary pressures of 18-19 GPa and temperatures in the range ~1900-2000 K. These conditions are unfavorable for the stabilization of bridgmanite, and implies that the lower mantle of Mars is mineralogically comparable to Earth’s mantle transition zone. This means that a relatively dense and thermally insulating lower mantle is absent in Mars, which favors the development of an early thermally-driven dynamo as a means of explaining crustal magnetism because of elevated core heat flux (*1*, *49*, *50*).

In agreement with geodetic observations that require a liquid core (*10*), the observation of ScS with significant relative amplitudes compared to direct S-waves rules out a solid outer core, because reflection coefficients would be too small at a solid-solid interface (fig. S6-2, (*38*)). The separate inversions converge on the same mean radius but show more spread in mean core density (Fig. 2C), which reflects the trade-off with mantle density through bulk mantle composition (indicated by the blue circles in Fig. 1C). Based on the distributions, we estimate core radius to be 1830±40 km, at the upper end of pre-mission estimates (*4*, *8*, *15*, *16*) that were based on an earlier and slightly lower degree-2 Love number (0.169±0.006, (*51*)), while mean core density lies in the range 5.7-6.3 g/cm$^3$. We also conducted separate inversions using the geodynamic method to consider the influence of individual data sets on the retrieved core properties (*38*). These inversions showed that the mean core radius changed from 1836 km (seismic data only) to 1815 km (geodetic data only), while the mean core density remained unchanged. To test the influence of the source depth, we fixed it to 50 km for all events, consistent with (*29*, *32*), and found that this would change the core radius to 1820±40 km, which is similar to the above range.

Compositional constraints on the core typically derive from geochemical models coupled with metal-silicate partitioning and mass balance arguments (*52–55*), but depend on the assumed compositions of the building blocks (*56*, *57*). While S is commonly considered the main light element (*14*, *44*, *45*, *55*) because of its abundance in the mantle as determined from the Martian meteorites (*58*) and its siderophile nature at the P-T-$fO_2$ conditions of the formation of Mars's core (*59*), additional light elements, including C, O, Si, N, and H are all potentially viable candidates as in Earth's core (*60–63*). Ni is also expected to be a core constituent based on meteorite compositions (*64*) and should make up ~5-6 wt% (*4*). The purple-shaded areas in Fig. 2C indicate how the mean core density varies with S content in the Fe-S, Fe-S-O, Fe-S-O-H, and Fe-S-O-H-C systems, based on thermodynamic solution models constructed using experimental data (*65–68*). For a core composed of Fe and S, sulfur contents surpass 25 wt%, which is above the value of the sulfur-richest meteorites (EH chondrites) and in excess of what is deduced from geo- and cosmochemical models (<13-19 wt.%, (*52*, *55*)). To bring the S content in line with the cosmochemical constraints, additional light elements (e.g., C, O, H) in the core are needed, see S11 (*38*). For geochemically defensible amounts of S, O, and H, the mean core density has to be >6 g/cm$^3$, which encompasses the upper end of our predictions (Fig. 2C). Because our core density is tied to reasonable assumptions about the composition and temperature of the Martian mantle, a higher mean core density is possible, that requires less light elements as a result of a lower bulk mantle FeO content (*46*) or higher temperatures as seen in some geodynamic models (*69*). The influence of a lower bulk mantle FeO content on mean core density is reflected by the cloud of blue circles with a mean core density >6.1 g/cm$^3$ (Fig. 2C) that were obtained on the basis of the bulk mantle composition of (*46*). Thus a lower bulk mantle FeO content seems to provide a better match than the canonical Martian compositions with FeO contents exceeding 17 wt% (*12*, *14*, *44*, *45*), which had also found to be at odds with geophysical constraints (*4*, *57*). As a preliminary observation, our results can be construed as pointing to an Fe-Ni core that is composed of, in order of abundance, S (10-15 wt.%), O (<5 wt.%), and H and C (<1 wt.% level) (*38*). While such O, H, and C contents represent upper limits, they serve to emphasize the need for light elements in Mars' core.

A chemical composition close to the eutectic (~15 wt.% S in the Fe-FeS binary at the core-mantle-boundary conditions of Mars) likely prevented crystallization of a bottom-up inner core because of the temperatures (~1200 K) required to drop below the liquidus (*70*). This is compatible with the absence of a current Martian geodynamo (*71*). Strong crustal remnant magnetization in the southern hemisphere of Mars (*72*) and observations of further magnetized units suggest a dynamo that was active between 4.5 Ga and 3.7 Ga (*9*). The dynamo would have been thermally-driven in the first few hundred Myr (*49*, *50*) and possibly followed by a compositionally-driven dynamo that may resuscitate through FeO exsolution (*73*) or inner-core crystallization (*71*, *74*, *75*). This, however, depends critically on the light element content and thermal state of the core.

As a consequence of the large core, the seismic core shadow on Mars (Fig. 3) commences at closer epicentral distances (94°-98°) than on Earth (100° (*76*)). This makes up half of the planet, including 33% of total extensional faults with 75% of those in terrain younger than 600 Ma (*77*). For Marsquakes in Tharsis, the region of Mars presumed to host most recent tectonic activity (*78*), direct P- and S-waves are therefore unobservable. That these events can therefore not be located easily, may result in an underestimation of the global seismic activity of Mars as seen from InSight's location (*27*).

The differentiation of Mars into a primordial crust, mantle, and core is likely the result of early magma ocean crystallization and solidification that could potentially result in compositional stratification of the mantle (*69*, *79*). There is, however, no direct evidence for this based on current observations. Continued analysis using marsquakes observed during the extended mission will be required to delve into the question of deep mantle layering. To determine the compressional wave speeds of the core itself, and further refine light element content, an unequivocal observation of an event beyond the core shadow, with clear core-crossing phases like PKP or SKS will be necessary. This would allow us to employ velocity-density systematics (*61*) as a means of gaining further insight into the total light element content of the core. In the interim, the new Martian seismic data and models presented here provide a wealth of new insights into the interior structure of Mars, which contain the clues needed to unravel the planetary building blocks (*57*), the physical and chemical conditions during assembly (*52*) and chronology of crust, mantle, and core formation (*25*).

**Materials and methods:**

The supplementary material consists of four main parts:

I. Sections 1-5, which present several complementary efforts to detect and characterize ScS arrivals;
II. Sections 6-7, which combines the ScS analyses and characterizes the corresponding environmental noise levels;
III. Sections 8-10, which describe the inversion for structural models;
IV. Section 11, which describes the implications of the structural models for Martian core composition.

References (88-124)

## References and Notes

1. D. J. Stevenson, *Nature*. **412**, 214–219 (2001).

2. M. T. Zuber *et al.*, *Science*. **287**, 1788–1793 (2000).

3. C. M. Bertka, Y. Fei, *Earth Planet. Sci. Lett.* **157**, 79–88 (1998).

4. A. Khan *et al.*, *J. Geophys. Res. Planets*. **123**, 1–37 (2018).

5. D. Breuer, D. A. Yuen, T. Spohn, *Earth Planet. Sci. Lett.* **148**, 457–469 (1997).

6. P. van Thienen, N. J. Vlaar, A. P. van den Berg, *Phys. Earth Planet. Inter.* **142**, 61–74 (2004).

7. T. Ruedas, P. J. Tackley, S. C. Solomon, *Phys. Earth Planet. Inter.* **216**, 32–58 (2013).

8. S. E. Smrekar *et al.*, *Space Sci. Rev.* **215**, 3–3 (2019).

9. A. Mittelholz, C. L. Johnson, J. M. Feinberg, B. Langlais, R. J. Phillips, *Sci. Adv.* **6**, eaba0513 (2020).

10. C. F. Yoder, A. S. Konopliv, D. N. Yuan, E. M. Standish, W. M. Folkner, *Science*. **300**, 299–303 (2003).

11. A. S. Konopliv *et al.*, *Geophys. Res. Lett.*, 0–2 (2020).

12. G. Dreibus, H. Wänke, in *Proceedings of the 27th International Geological Congress* (1984), vol. 11, pp. 1–20.

13. H. Y. McSween, K. Keil, *Geochim. Cosmochim. Acta*. **64**, 2155–2166 (2000).

14. G. J. Taylor, *Chem. Erde - Geochem.* **73**, 401–420 (2013).

15. A. Bagheri, A. Khan, D. Al-Attar, O. Crawford, D. Giardini, *J. Geophys. Res. Planets*. **124**, 2703–2727 (2019).

16. A. Rivoldini, T. Van Hoolst, O. Verhoeven, A. Mocquet, V. Dehant, *Icarus*. **213**, 451–472 (2011).

17. C. Hutton, *Philos. Trans. R. Soc. Lond.* (1778).

18. R. D. Oldham, *Q. J. Geol. Soc.* **62**, 456–475 (1906).

19. I. Lehmann, *Bur. Cent. Séismologique Int. Sér. Trav. Sci.* **14**, 87–115 (1936).

20. K. E. Bullen, *Phys. Chem. Earth*. **1**, 68–93 (1956).

21. C. G. Dahm, *Eos Trans. Am. Geophys. Union*. **15**, 80–83 (1934).

22. G. V. Latham *et al.*, *Science*. **174**, 687–92 (1971).

23. R. F. Garcia, J. Gagnepain-Beyneix, S. Chevrot, P. Lognonné, *Phys Earth Planet Inter*. **188**, 96–113 (2011).

24. R. C. Weber, P.-Y. Lin, E. J. Garnero, Q. Williams, P. Lognonne, *Science*. **331**, 309–312 (2011).

25. N. Dauphas, A. Pourmand, *Nature*. **473**, 489–492 (2011).

26. K. Mezger, V. Debaille, T. Kleine, *Space Sci. Rev.* **174**, 27–48 (2013).

27. W. B. Banerdt *et al.*, *Nat. Geosci.* **13**, 183–189 (2020).

28. P. Lognonné *et al.*, *Space Sci. Rev.* **215**, 12–12 (2019).

29. D. Giardini *et al.*, *Nat. Geosci.* **13**, 205–212 (2020).

30. InSight Marsquake Service, Mars Seismic Catalogue, InSight Mission; V6 2021-04-01 (2021), p. 12 MB, , doi:10.12686/A11.

31. P. Lognonné *et al.*, *Nat. Geosci.* **13**, 213–220 (2020).

32. A. Khan *et al.*, *Science*. **in revisio** (2021).

33. B. Knapmeyer-Endrun, M. P. Panning, et al., *Science*. **in revision**.

34. J. Taylor, N. A. Teanby, J. Wookey, *J. Geophys. Res. E Planets*. **118**, 2570–2581 (2013).

35. N. Brinkman *et al.*, *J. Geophys. Res. Planets* (2021), doi:10.1029/2020je006546.

36. M. Schimmel, J. Gallart, *Bull. Seismol. Soc. Am.* **94**, 1016–1035 (2004).

37. P. S. Schultz, J. F. Claerbout, *GEOPHYSICS*. **43**, 691–714 (1978).

38. "Materials and methods are available as supplementary materials at the Science website."

39. J.-R. Scholz *et al.*, *Earth Space Sci.* **7**, 1–31 (2020).

40. A.-C. Plesa *et al.*, *J. Geophys. Res. Planets*, in press, doi:10.1029/2020JE006755.

41. M. Drilleau, H. Samuel, A. Rivoldini, M. Panning, P. Lognonné, *Geophys. J. Int.* (2021), doi:10.1093/gji/ggab105.

42. H. Samuel, P. Lognonné, M. P. Panning, V. Lainey, *Nature*. **569**, 523–527 (2019).

43. A. Khan, J. A. D. Connolly, *J. Geophys. Res.* **113**, E07003–E07003 (2008).

44. K. Lodders, B. Fegley, *Icarus*. **126**, 373–394 (1997).

45. C. Sanloup, A. Jambon, P. Gillet, *Phys. Earth Planet. Inter.* **112**, 43–54 (1999).

46. T. Yoshizaki, W. F. McDonough, *Geochim. Cosmochim. Acta*. **273**, 137–162 (2020).

47. C. B. Agee, D. S. Draper, *Earth Planet. Sci. Lett.* **224**, 415–429 (2004).

48. K. Mosegaard, A. Tarantola, *J. Geophys. Res.* **100**, 12431–12431 (1995).

49. D. Breuer, T. Spohn, *J. Geophys. Res.* **108**, 5072–5072 (2003).

50. J.-P. Williams, F. Nimmo, *Geology*. **32**, 97–97 (2004).

51. A. S. Konopliv, R. S. Park, W. M. Folkner, *Icarus*. **274**, 253–260 (2016).

52. M. C. Brennan, R. A. Fischer, J. C. E. Irving, *Earth Planet. Sci. Lett.* **530**, 115923 (2020).

53. K. Righter, N. L. Chabot, *Meteorit. Planet. Sci.* **46**, 157–176 (2011).

54. D. C. Rubie *et al.*, *Icarus*. **248**, 89–108 (2015).

55. E. S. Steenstra, W. van Westrenen, *Icarus*. **315**, 69–78 (2018).

56. C. Fitoussi, B. Bourdon, X. Wang, *Earth Planet. Sci. Lett.* **434**, 151–160 (2016).

57. C. Liebske, A. Khan, *Icarus*. **322**, 121–134 (2019).

58. G. Dreibus, H. Wanke, *Meteoritics*. **20**, 367–381 (1985).

59. N. Rai, W. van Westrenen, *J. Geophys. Res. Planets*. **118**, 1195–1203 (2013).

60. J. Badro, J. P. Brodholt, H. Piet, J. Siebert, F. J. Ryerson, *Proc. Natl. Acad. Sci.* **112**, 12310–12314 (2015).

61. F. Birch, *J. Geophys. Res. 1896-1977*. **69**, 4377–4388 (1964).

62. J.-P. Poirier, *Phys. Earth Planet. Inter.* **85**, 319–337 (1994).

63. V. N. Zharkov, *Sol. Syst. Res.* **30**, 456 (1996).

64. A. E. Ringwood, *Geochem. J.* **11**, 111–135 (1977).

65. J. V. Badding, H. K. Mao, R. J. Hemley, (American Geophysical Union, 2013), pp. 363–371.

66. T. Komabayashi, *J. Geophys. Res. Solid Earth*, 2014JB010980 (2014).

67. G. Morard *et al.*, *Am. Mineral.* (2018).

68. H. Terasaki *et al.*, *J. Geophys. Res. Planets*. **124** (2019).

69. L. T. Elkins-Tanton, E. M. Parmentier, P. C. Hess, *Meteorit. Planet. Sci.* **38**, 1753–1771 (2003).

70. Y. Mori *et al.*, *Earth Planet. Sci. Lett.* **464**, 135–141 (2017).

71. A. J. Stewart, M. W. Schmidt, W. Van Westrenen, C. Liebske, *Science*. **316**, 1323–1325 (2007).

72. M. H. Acuña *et al.*, *Science*. **284**, 790–793 (1999).

73. K. Tsuno, E. Ohtani, H. Terasaki, *Phys. Earth Planet. Inter.* **160**, 75–85 (2007).

74. D. Breuer, W. B. Moore, in *Treatise on Geophysics (Second Edition)*, G. Schubert, Ed. (Elsevier, Oxford, Second Edi., 2015), pp. 255–305.

75. D. J. Hemingway, P. E. Driscoll, *J. Geophys. Res. Planets*, in press, doi:https://doi.org/10.1029/2020JE006663.

76. B. L. N. Kennett, E. R. Engdahl, *Geophys. J. Int.* **105**, 429–465 (1991).

77. M. Knapmeyer *et al.*, *J. Geophys. Res. E Planets*. **111**, 1–23 (2006).

78. R. C. Anderson *et al.*, *J. Geophys. Res. Planets*. **106**, 20563–20585 (2001).

79. H. Samuel *et al.*, *J. Geophys. Res. Planets*, in press, doi:https://doi.org/10.1029/2020JE006613.

80. J. D. Hunter, *Comput. Sci. Eng.* **9**, 90–95 (2007).

81. L. Krischer *et al.*, *Comput. Sci. Discov.* **8**, 014003–014003 (2015).

82. C. R. Harris *et al.*, *Nature*. **585**, 357–362 (2020).

83. P. Virtanen *et al.*, *Nat. Methods*. **17**, 261–272 (2020).

84. InSight Mars SEIS Data Service, *SEIS raw data, Insight Mission* (IPGP, JPL, CNES, ETHZ, ICL, MPS, ISAE-Supaero, LPG, MFSC, 2019; http://datacenter.ipgp.fr/networks/detail/XB_2016).

85. S. C. Stähler, A. Khan, M. Drilleau, A. C. Duran, H. Samuel, Interior Models of Mars from inversion of seismic body waves (2021), (available at doi:10.18715/IPGP.2021.kpmqrnz8).

86. A. G. Marusiak, N. C. Schmerr, M. E. Banks, I. J. Daubar, *Icarus*. **335**, 113396 (2020).

87. D. E. Smith *et al.*, *J. Geophys. Res. Planets*. **106**, 23689–23722 (2001).

88. J. F. Clinton *et al.*, *Space Sci. Rev.* **214**, 133–133 (2018).

89. R. G. Stockwell, L. Mansinha, R. P. Lowe, *IEEE Trans. Signal Process.* **44**, 998–1001 (1996).

90. S. Greenhalgh, D. Sollberger, C. Schmelzbach, M. Rutty, in *Advances in Geophysics*, C. Schmelzbach, Ed. (Elsevier, 2018; https://www.sciencedirect.com/science/article/pii/S0065268718300025), vol. 59, pp. 123–170.

91. J. C. Samson, *Geophys. J. Int.* **72**, 647–664 (1983).

92. E. Stutzmann *et al.*, *J. Geophys. Res. Planets*. **126** (2021), doi:10.1029/2020JE006545.

93. J. Park, F. L. Vernon, C. R. Lindberg, *J. Geophys. Res. Solid Earth*. **92**, 12664–12674 (1987).

94. K. D. Koper, V. L. Hawley, *Earthq. Sci.* **23**, 439–447 (2010).

95. P. J. Goodling, V. Lekic, K. Prestegaard, *Earth Surf. Dyn.* **6**, 351–367 (2018).

96. E. Galetti, A. Curtis, *Tectonophysics*. **532–535**, 1–26 (2012).

97. M. Schimmel, *Bull. Seismol. Soc. Am.* **89**, 1366--1378 (1999).

98. J. F. Clinton *et al.*, *Phys. Earth Planet. Inter.* **310** (2021), doi:10.1016/j.pepi.2020.106595.

99. M. M. Haney *et al.*, *Bull. Volcanol.* **82**, 18 (2020).

100. N. Compaire *et al.*, *J. Geophys. Res. Planets*, in press, doi:https://doi.org/10.1029/2020JE006498.

101. M. Schimmel, E. Stutzmann, J. Gallart, *Geophys. J. Int.* **184**, 494–506 (2011).

102. S. Ceylan *et al.*, *Phys. Earth Planet. Inter.* **310**, 106597–106597 (2021).

103. J. F. Montalbetti, E. R. Kanasewich, *Geophys. J. Int.* **21**, 119–129 (1970).

104. S. Rost, C. Thomas, *Rev. Geophys.* **40**, 1008–1008 (2002).

105. J. F. Clinton *et al.*, *Seismol. Res. Lett.* **88**, 1290–1302 (2017).

106. G. Prieto, R. L. Parker, F. L. Vernon, *Comput. Geosci.* **35**, 1701–1710 (2009).

107. J. N. Brune, *J. Geophys. Res.* **75**, 4997–5009 (1970).

108. G. Nolet, *A breviary of seismic tomography: imaging the interior of the earth and sun* (Cambridge University Press, 2008; www.cambridge.org/9780521882446).

109. C. Charalambous *et al.*, *J. Geophys. Res. Planets*, in press, doi:10.3929/ethz-b-000479669.

110. R. F. Garcia *et al.*, *J. Geophys. Res. Planets*, in press, doi:https://doi.org/10.1029/2019JE006278.

111. J. a. D. Connolly, *Geochem. Geophys. Geosystems*. **10** (2009), doi:https://doi.org/10.1029/2009GC002540.

112. L. Stixrude, C. Lithgow-Bertelloni, *Geophys. J. Int.* **162**, 610–632 (2005).

113. L. Stixrude, C. Lithgow-Bertelloni, *Geophys. J. Int.* **184**, 1180–1213 (2011).

114. J. A. D. Connolly, A. Khan, *Geophys. Res. Lett.* **43**, 5026–5034 (2016).

115. M. Drilleau *et al.*, *Earth Space Sci.*, in press, doi:https://doi.org/10.1029/2020EA001118.

116. S. ~R. Taylor, S. McLennan, *Planetary Crusts: Their Composition, Origin and Evolution* (2009).

117. J. ~A. ~D. Connolly, *Earth Planet. Sci. Lett.* **236**, 524–541 (2005).

118. A. Khan, K. Mosegaard, J. G. Williams, P. Lognonné, *J. Geophys. Res. Planets*. **109**, 9007–9007 (2004).

119. H. P. Crotwell, T. J. Owens, J. Ritsema, *Seismol. Res. Lett.* **70**, 154–160 (1999).

120. K. Tsuno, D. S. Grewal, R. Dasgupta, *Geochim. Cosmochim. Acta*. **238**, 477–495 (2018).

121. I. Blanchard, J. Badro, J. Siebert, F. J. Ryerson, *Earth Planet. Sci. Lett.* **427**, 191–201 (2015).

122. J. G. O'Rourke, S.-H. Shim, *J. Geophys. Res. Planets*. **124**, 3422–3441 (2019).

123. Y. Shibazaki, E. Ohtani, H. Terasaki, A. Suzuki, K. Funakoshi, *Earth Planet. Sci. Lett.* **287**, 463–470 (2009).

124. G. Morard *et al.*, *J. Geophys. Res. Solid Earth*. **122**, 7813–7823 (2017).

## Acknowledgments:

This is InSight contribution 200.

We acknowledge NASA, CNES, partner agencies and Institutions (UKSA, SSO, DLR, JPL, IPGP-CNRS, ETHZ, IC, MPS-MPG) for the development of SEIS. The Swiss contribution in implementation of the SEIS electronics was made possible through funding from the federal Swiss Space Office (SSO), the contractual and technical support of the ESA-PRODEX office. Numerical simulations were supported by a grant from the Swiss National Supercomputing Centre (CSCS) under project ID s922, as well as HPC resources of CINES under the allocation A0090407341, made by GENCI. We thank Boris Dintrans, director of CINES, for his efficient handling of our request for computational time. Figures were created using matplotlib (*80*), seismic data processing in ObsPy (*81*), numerical evaluation in NumPy and SciPy (*82*, *83*).

**Funding:**

S.C.S., A.K., D.G., J.C., A.C.D., G.Z., and N.D. acknowledge support from ETHZ the ETH+ funding scheme (ETH+2 19-1: “Planet MARS”).

W.B.B., A.G.M., M.P.P., and S.E.S. were supported by the NASA InSight mission and funds from the Jet Propulsion Laboratory, California Institute of Technology, under a contract with the National Aeronautics and Space Administration (80NM0018D0004).

D.A. has received funding from the European Research Council (ERC) under the European Union’s Horizon 2020 research and innovation Programme (Grant agreement 724690).

The French teams acknowledge support from CNES as well as Agence Nationale de la Recherche (ANR-14-CE36-0012-02 and ANR-19-CE31-0008-08).

A. R. was financially supported by the Belgian PRODEX program managed by the European Space Agency in collaboration with the Belgian Federal Science Policy Office.

M.S. wishes to thank SANIMS (RTI2018-095594-B-I00).

M.V.D. received support from the European Research Council (ERC) under the EU’s Horizon 2020 programme (grant No. 714069).

D.S. and C.S. acknowledge funding from ETH Research grant ETH-06 17-02.

J.C.E.I. acknowledges support from NASA grant 80NSSC18K1633.

N.S, D.K., Q.H., R.M., V.L., and A.G.M. acknowledge NASA grant 80NSSC18K1628 for support.

V.L. acknowledges support from the Packard Foundation.

A.H. was funded by the UK Space Agency (grant ST/R002096/1).

A.-C.P. acknowledges the financial support and endorsement from the DLR Management Board Young Research Group Leader Program and the Executive Board Member for Space Research and Technology.

**Author contributions:**

S.C.S, D.G. S.C, R.G., Q.H., D.K. V.L., M.S., N.S., D.S., É.S., C.S., G.Z. analyzed the seismic data and made arrival time picks.

S.C.S., P.L., D.G., Z.X., C.C. and W.T.P. performed the statistical analysis of the observed signals.

S.C.S., Q.H., N.S., R.M. and A.G.M. identified the arrivals as ScS based on interior models from A.K., H. S. and A.R..

A.K., M.D., A.C.D. and H.S. performed the inversions.

S.C.S., A.K., P.L., D.G., D.A., J.C.E.I., M.K., C.P. A-C.P., A.R., T.G., and S.E.S. participated and contributed to the interpretation of the results.

Review of the continuous data and detection of marsquakes was done by S.C.S., S.C., G.Z, N.D., J.F.C., M.P. and A.H. with operational support by É.B. and P.D..

S.C.S. and A.K. wrote the paper with contributions from H.S., N.S., D.A., J.C.E.I., A.G.M., A-C.P., A.R., J.C. and M.v.D.

J.C.E.I., R.M., M.K. and V.L. reviewed the contributions to the supplementary material.

The InSight mission is managed by W.B.B., M.P.P., and S.E.S.

The SEIS instrument development was led by P.L., D.G., and W.T.P.

Supplementary section 1 was written by M.S., D.S. and É.S. with contributions from S.C.S., C.S., and Z.X.

Supplementary section 2 was written by D.K. and V.L. with contributions from J.C.E.I., and N.S.

Supplementary section 3 was written by M.S. and É.S.

Supplementary section 4 was written by R.G. with contributions from M.D.

Supplementary section 5 was written by Q.H. with contributions from N.S.

Supplementary section 6 was written by S.C.S. with contributions from the authors of the other supplements.

Supplementary section 7 was written by Z.X. and C.C. with contributions from P.L. and W.T.P.

Supplementary section 8 was written by A.K., M.D, A.C.D., and H.S.

Supplementary section 9 was written by M.D.

Supplementary section 10 was written by A.C.D, A.K., and M.D.

Supplementary section 11 was written by D.A. and A.R, with contributions from A.K.

**Competing interests:** Authors declare that they have no competing interests.

**Data and materials availability:** We thank the operators of JPL, SISMOC, MSDS, IRIS-DMC and PDS for providing SEED SEIS data (*84*). 300 interior models derived in this study are available as electronic supplement (*38*) and from (*85*).

## Figures

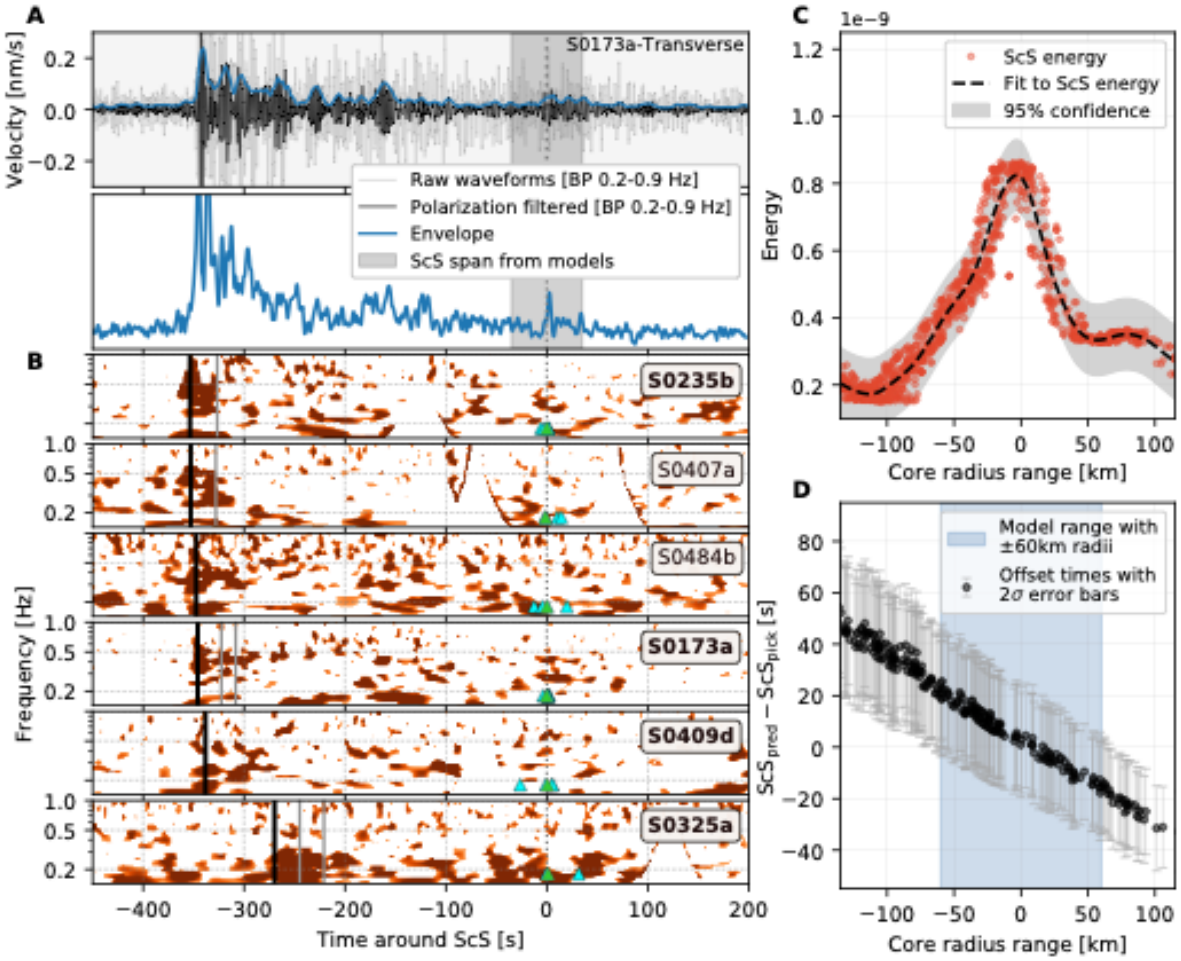


**Fig. 1. Summary of data processing and identification of core-reflected S-waves.** (**A**) Seismogram and envelope of event S0173a before and after polarization filtering (top) and envelope stack for all six events (bottom). The individual event envelopes are shown in Fig. S1-4 (*38*). (**B**) Polarization-filtered spectrograms for each of the six events considered here. Cyan triangles mark proposed ScS picks based on the processing methods described in the main text, whereas green triangles mark the final set of picks summarized in Table 1. Light grey lines mark SS and SSS picks from (*32*). All events show energy around the predicted arrival time of ScS, using a model from (*32*) with a core radius of 1830 km, in agreement with the ScS observation for S0173a shown in (**A**). Bold event labels (e.g., S0235b) indicate events with strong ScS energy. (**C**) Stacked energy in a 10 s time window around ScS as predicted for 5000 models from (*32*) with core radii centered around 1830. (**D**) Residual travel times of the models presented in

(**C**) compared to the picks in (**B**), show that the ScS picks are able to constrain the core radius to within ±60 km (*86*).

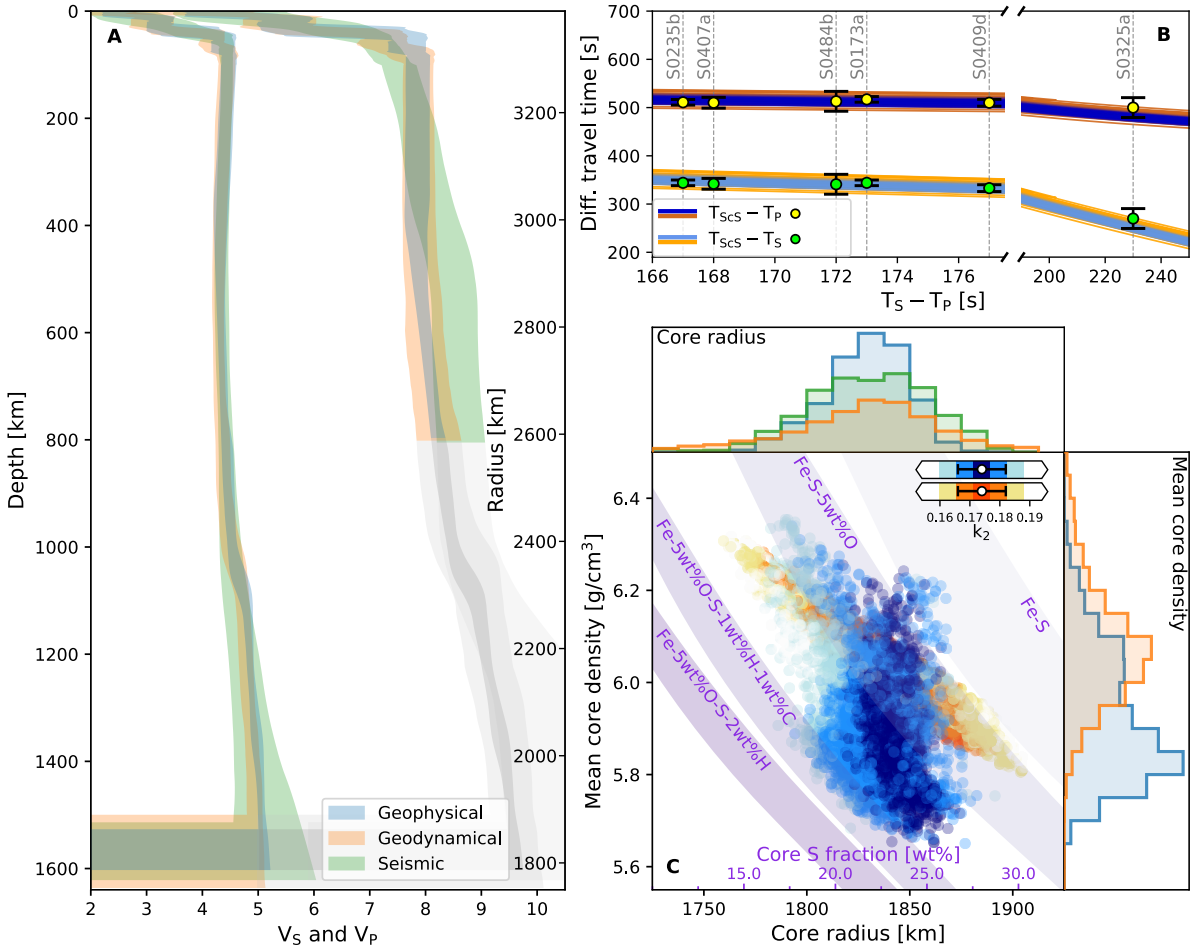


**Fig. 2. Mars's mantle and core structure.** (**A**) Inverted seismic wave velocity profiles (95% credible intervals) based on the three inversion methods. The pale gray-shaded area below 800 km depth for the P-wave velocity profiles indicates that no direct information is available for this region. (**B**) Differential body wave travel time misfits for all sampled models obtained from the geophysical (blue shades) and geodynamical (orange shades) inversions shown in panel (**A**). Yellow and green circles indicate the observations including error bars, respectively. A detailed version of the misfit plot is shown in Figure S9-1 (*38*). (**C**) Sampled core properties. Middle plot: mean core density versus core radius for the geophysical (blue) and geodynamical (orange) methods, while their marginal distributions are shown as histograms to the right and on the top. The seismic method only constrains core radius. The blue and orange models are color-coded according to their fit to the tidal response in the form of the observed degree-2 Love number $k_2$ (*11*) defined by the white circles and horizontal error bars. Relying on Fe-S models, the purple bands indicate the variation of core sulfur (S) content (purple axis) with mean core density for four different iron (Fe) - light element (S, O, H, and C) assemblages (*65–68*).

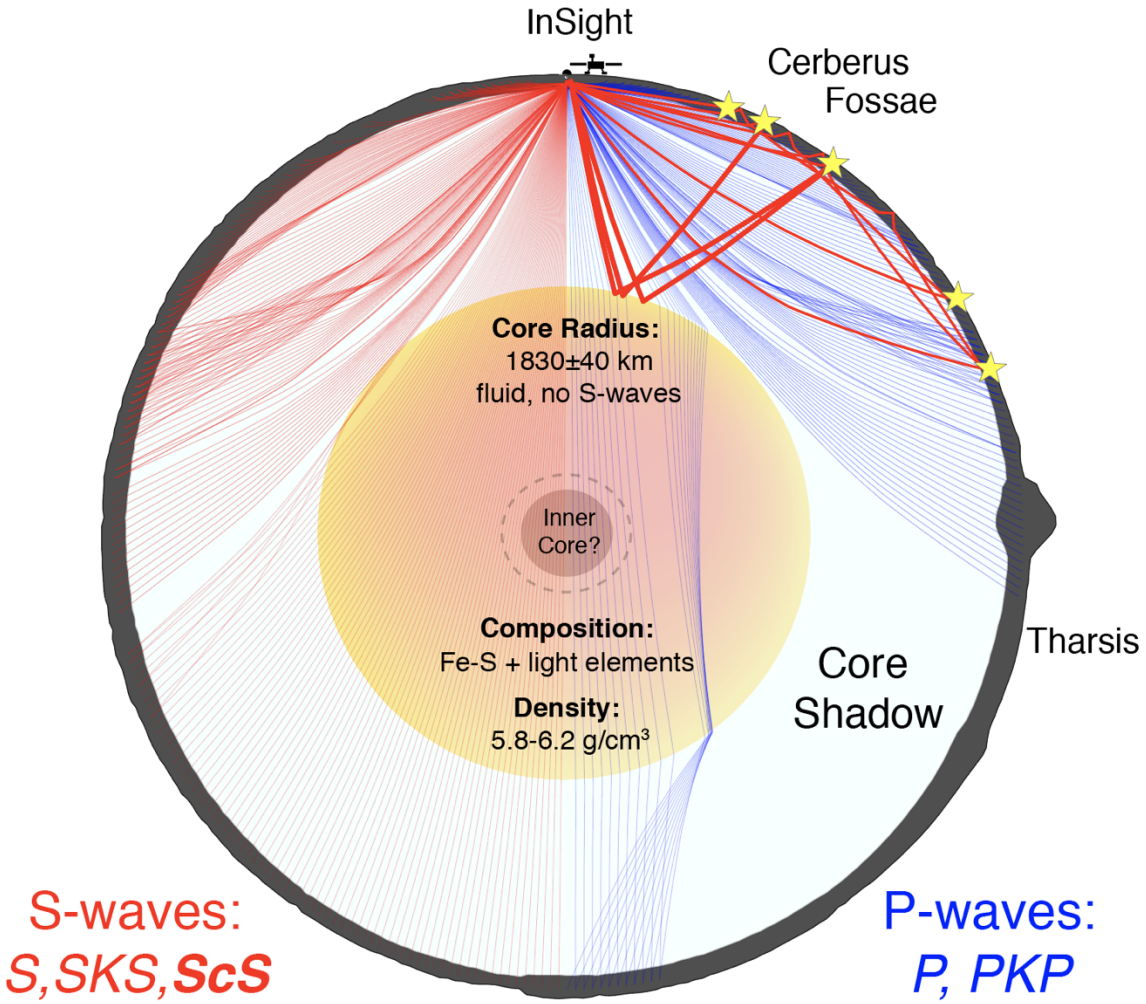


**Fig. 3. Schematic diagram of Mars's interior structure.** The cross section depicts the core-induced shadow zone for seismic waves. The surface topography is a cut through the MOLA map (*87*) on a great circle arc from InSight through Olympus Mons. The S-wave shadow zone is minimal and probably filled by diffracted S-waves (Sdiff), while the P-wave shadow zone is significant and contains specifically the Tharsis region. The existence of an inner core cannot be determined by current data and the seismic ray paths shown assume no inner core. Topography and InSight lander are exaggerated in scale.

| Event | tS-tP [sec] | tScS - tP [sec] | sigma(tScS) | depth [km] | $M_w$ |
|---|---|---|---|---|---|
| S0235b | 167 | 511 | 3 | 24±5 | 3.5 |
| S0407a | 168 | 510 | 10 | 25±5 | 3.0 |
| S0484b | 172 | 513 | 20 | 33±5 | 2.9 |
| S0173a | 173 | 512 | 3 | 24±5 | 3.6 |
| S0409d | 177 | 510 | 5 | 25±5 | 3.1 |
| S0325a | 230 | 500 | 20 | 30±5 | 3.7 |

**Table 1: Consolidated pick times of P and ScS for the events used in this study.**
Magnitudes are from the MQS catalog v6 (*30*). Depth estimates are based on the identification of the depth phase sS (see the main text). The events are labelled by mission Sol of occurrence and sub-labeled alphabetically for Sols with more than 1 event.